Supplementary Material

S1 Extraction of PCC/precuneus seeds associated with the DMN

S1.1 Parcellation of PCC/precuneus

Voxels within the left/right PCC and precuneus delineated by the AAL atlas (~7500 voxels in total at 2mm isotropic resolution, see Fig. S1(A) below) were clustered into multiple functional units based on their functional connectivity with the rest of gray matter ROIs (112 ROIs derived from AAL atlas excluding PCC/precuneus). Clustering analysis was firstly performed for each individual separately, and the results were combined later to yield a group-level parcellation.

At the individual level, parcellation of the PCC/precuneus was implemented by K-means clustering prior to spatial smoothing and normalization to MNI space: the observation series was the linear Pearson correlation between each PCC/precuneus voxel and the averaged time series within each rest gray matter ROI; the distance metric between two voxels was defined as 1 minus the linear Pearson correlation between their corresponding observation series. The number of clusters k was varied from 2 to 8, and the K-means clustering was repeated 50 times for each.

The group level parcellation was achieved by synthesizing the K-means clustering results from the individual-subject analysis (50 trials per subject, 1000 trials in total for 20 subjects) via the Normalized-cut method (http://www.cis.upenn.edu/~jshi/software/), where the weighting between two voxels i and j is defined as:

$$w_{i,j} = \sum_{n=1}^{1000} I_n(i,j \in \textit{same cluster})$$

where I is the indicator function (i.e., $I = 1$ if $i,j \in \textit{same cluster}$, $I = 0$ otherwise), n is the nth trial of the K-means clustering.

The RAND index (Rand, 1971) (a widely used metric to evaluate the similarity between different partition results, ranging from 0 (entirely different partition) to 1 (identical partition)) was used to compare the similarity between the parcellation results associated with different cluster number ks.

For two sets of partition results P_1, P_2, RAND index R is computed as:

$$R = \frac{a+b}{a+b+c+d}$$

$$\mathrm{a} = \sum_{\mathrm{i,j}} \mathrm{I}\{\text{voxel i,j} \in \text{same cluster in } P_1 \;\&\; \text{voxel i,j} \in \text{same cluster in } P_2\}$$

$$\mathrm{b} = \sum_{\mathrm{i,j}} \mathrm{I}\{\text{voxel i,j} \notin \text{same cluster in } P_1 \;\&\; \text{voxel i,j} \notin \text{same cluster in } P_2\}$$

$$\mathrm{c} = \sum_{\mathrm{i,j}} \mathrm{I}\{\text{voxel i,j} \in \text{same cluster in } P_1 \;\&\; \text{voxel i,j} \notin \text{same cluster in } P_2\}$$

$$\mathrm{d} = \sum_{\mathrm{i,j}} \mathrm{I}\{\text{voxel i,j} \notin \text{same cluster in } P_1 \;\&\; \text{voxel i,j} \in \text{same cluster in } P_2\}$$

As reflected in Fig. S1(B), the differences between different cluster numbers became very minor when *k* approached *5* (RAND index ~0.90), i.e. major functional components remained unaltered while small, disconnected components further split for *k = 6~8*. Further inspection of the parcellation results associated with *k = 4* and *k = 5* (Fig. S1(C)) revealed that only one cluster showed a noticeable difference between these two settings; specifically, the region in yellow (see '*k = 4'* panel, *white arrow*) encompassed an additional small cluster when *k=5* (see '*k =5'* panel, *white arrows.*). Based on this analysis, the parcellation results of *k = 4* was considered representative of the major functional components within PCC/precuneus.

S1.2 Cluster centroids as PCC/precuneus seeds

Cluster centroids of two of the four resolved functional units (Fig. S1(C), *k = 4*, green and yellow) were considered to be DMN related and chosen as the seeds for further comparison of PCC/precuneus positive/negative correlations. The MNI coordinates of the selected two seeds (denoted as *SEED1/SEED2* in Fig. S1(C), 6 mm radius sphere) are [0, -60, 46] and [0, -50, 26] respectively. The black cluster was not included due to its fragmentary configuration. The superior cluster (Fig. S1(C) blue) was excluded, because regions significantly correlated with the cluster centroid did not contain core nodes within the DMN, e.g. MPFC, bilateral parietal cortex (see Fig. S1(D) for the functional connectivity map, the analysis was the same as section 2.5 Functional connectivity with respect to *SEED1/SEED2* below).

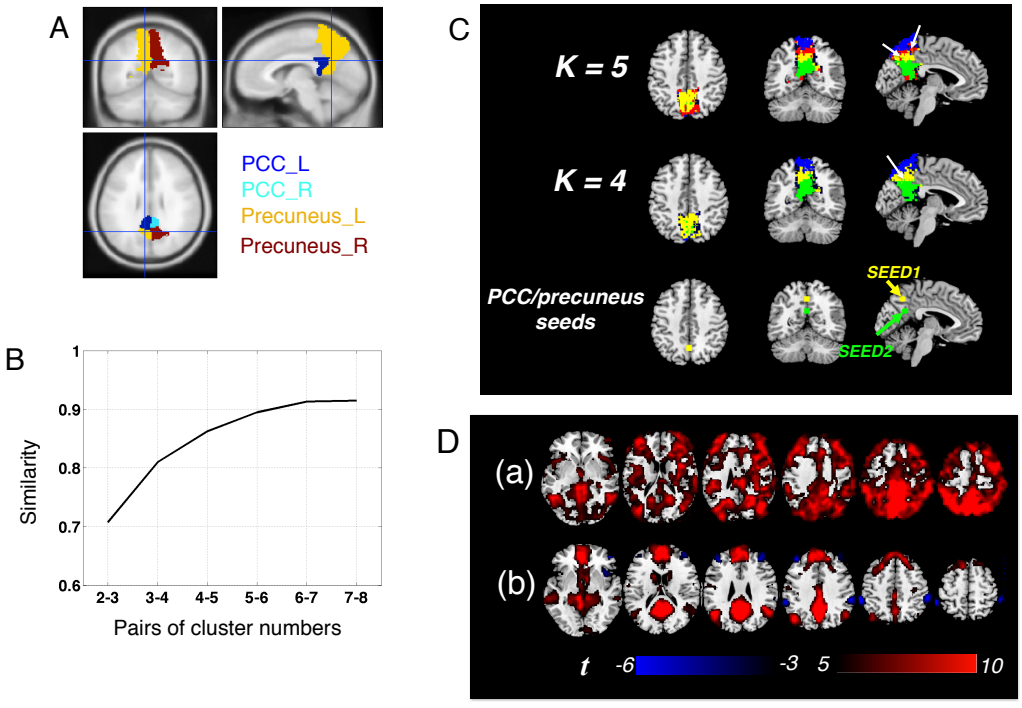

Fig. S1 Illustration of PCC/precuneus parcellation. (A) Anatomical regions included for PCC parcellation; (B) Similarity (RAND index) between adjacent cluster number pairs (e.g. 2-3, the similarity between the parcellation results associated with K-means clustering number $k = 2$ and $k = 3$); (C) Sub functional units of PCC/precuneus revealed by clustering (top two rows, cluster number k = 4/5, different clusters are illustrated by distinct colors) and the selected seeds (bottom row, centroids of two clusters when k = 4, colored in yellow and green); (D) Group-level t map of regions positively/negatively correlated with the centroid of a superior precuneus cluster (C, $k = 4$, blue) (a), core nodes within DMN, e.g. MPFC, bilateral IPL are not included. Correlation map with respect to *SEED2* is shown in (b) for comparison.

S1.3 Comparison of PCC/precuneus parcellation to prior studies

Compared to the reported functional division of posteromedial cortex (PMC) by other studies, (1) the functional unit of *SEED1* mainly overlaps with the cognitive subnetwork in (Margulies et al., 2009), task-negative and visual subnetworks in (Cauda et al., 2010), cluster 4 (a transition zone between dorsal and ventral PMC) and part of cluster 2-3 (dorsal PMC) in (Zhang et al., 2014); (2) the functional unit of *SEED2* overlaps with the limbic subnetwork in (Margulies et al., 2009), task-negative network in (Cauda et al., 2010), and cluster 5 (DMN) in (Zhang et al., 2014). An anterior-posterior dissociation of the superior part of precuneus (Fig. S1(C), $k = 4$, dark blue) as reported in (Cauda et al., 2010; Margulies et al., 2009; Zhang et al., 2014) emerged when $k \geq 6$. Inconsistent clustering results between our study and the discussed groups may be attributed to different clustering methodology/metrics employed: Margulies et al. and Cauda et al. parcellated the PMC ROIs/voxels based on the similarity of BOLD time series, they used spectral clustering and fuzzy clustering respectively; Zhang et al. parcellated the PMC based on each voxel's structual connectivity (obtained with diffusion tensor imaging) with the whole brain, the spectral clustering approach was applied. Also, the anatomical regions included in these studies are more spatially extensive compared to the PCC/precuneus delineated by AAL atlas (those manually selected PMC regions further include the retrosplenial cortex for clustering, and expand more in anterior/posterior directions).

However, although different studies obtain slightly inconsistent results pertaining to how PCC/precuneus connect with extensive resting state networks, they converge on the conclusion that only the ventral part of the PCC/precuneus associates with the DMN. This is also demonstrated by the linear correlation analysis in our dataset: central nodes of the DMN correlate with both *SEED1* and *SEED2* (both of which were situated in the ventral part of PCC/precuneus), but not with the centroid of a superior cluster (Fig. S1(D)). Thus, the selected two clusters may be adequate for the primary focus of our study, which is to differentiate anti-correlated networks of the DMN.

S2 Point-process analysis of *SEED1/SEED2*

S2.1 Point-process analysis of *SEED1/SEED2*

Point-process analysis was performed on the data preprocessed by steps described in section 2.2. We first transformed each subject's dataset to z-scores (the time series of each voxel was demeaned and normalized by its temporal standard deviation), and extracted two sets of temporal frames '*TF1*', defined as (*SEED1* z-score > 1 & *SEED2* z-score < 1) and '*TF2*', defined as (*SEED2* z-score > 1 & *SEED1* z-score < 1). Spatial maps within each temporal frame set *TF1* and *TF2* were averaged for each subject and then entered into a Wilcoxon signed-rank test to assess statistical significance (see S2.2 justifications of the non-parametric test), yielding co-activation patterns (CAPs) solely associated with *SEED1* (*SEED1-CAP*) and *SEED2* (*SEED-CAP*).

The numbers of time frames sorted into the sets *TF1* and *TF2* are 20±7 and 20±6 (mean±SD across 20 subjects) respectively, which each represent about 8.3% of the total scan time (see supplementary Table S1 for detailed information for each subject).

The analyses were motivated by the recent proposal that transient co-activation between regions can be explored by averaging over a few critical time frames when the seed signal exhibits relatively large BOLD signal fluctuations. We therefore further inferred that focusing on time series points when only a single functional unit is 'active' (z-score > 1), would reveal network patterns associated uniquely with each seed.

S2.2 Null distributions of the point-process analysis

In the point process analysis, spatial maps of those time frames during which a seed voxel's amplitude is higher than 1 s.d. are averaged. The null distribution of each voxel's averaged signal amplitude varies as a function of the number of averaged time frames k and its temporal correlation with the reference seed ρ.

For simplicity, let's assume that post z-score transformation, the seed time series X and a random voxel's time series Y are i.i.d., following a joint Gaussian distribution: $\mathbb{N}\left(\begin{bmatrix}0\\0\end{bmatrix},\begin{bmatrix}1 & \rho\\ \rho & 1\end{bmatrix}\right)$. Let's further assume that there exists k time frames when the amplitudes of the seed voxel are > 1.

When k = 1, $\overline{Y_k}$, the averaged signal amplitude of time series Y is non-Gaussian, following:

$$P(\overline{Y_k}) = \frac{\int_1^{+\infty} f(Y|X)dX}{\int_1^{+\infty} f(X)dX}$$

$$\text{where } Y|(X=x) \sim \mathbb{N}\left(\rho x, (1-\rho^2)\right), and\ X \sim \mathbb{N}(0,1)$$

When $k \to \infty$, $\overline{Y_k} \to \mathbb{N}(1.53\rho, \frac{1-0.8\rho^2}{k})$ according to the central limit theorem.

Thus, for sufficiently large k, $\overline{Y_k}$ approximates Gaussian and the hypothesis $\{\overline{Y_k} \neq 0\}$ can be examined via a simple student's t test; however for small ks, t test won't be valid.

In the present study, k is 20 on average (see section 3.3 in the main text), null

distributions of $\overline{Y_k}$ under various ρs are simulated in Fig. S2.1. Clear discrepancy between a standard Gaussian distribution (mean = 0, stdev = 1) and the scaled distributions of $\overline{Y_k}$ estimated from monte carlo simulations can be observed, if $|\rho|$ is sufficiently large. Given that ρs of different brain voxels span a broad range of values, which may not be well approximated by Gaussian distributions, the non-parametric Wilcoxon signed-rank test was employed to assess the statistical significance of $\overline{Y_k}$ against 0 in the present study.

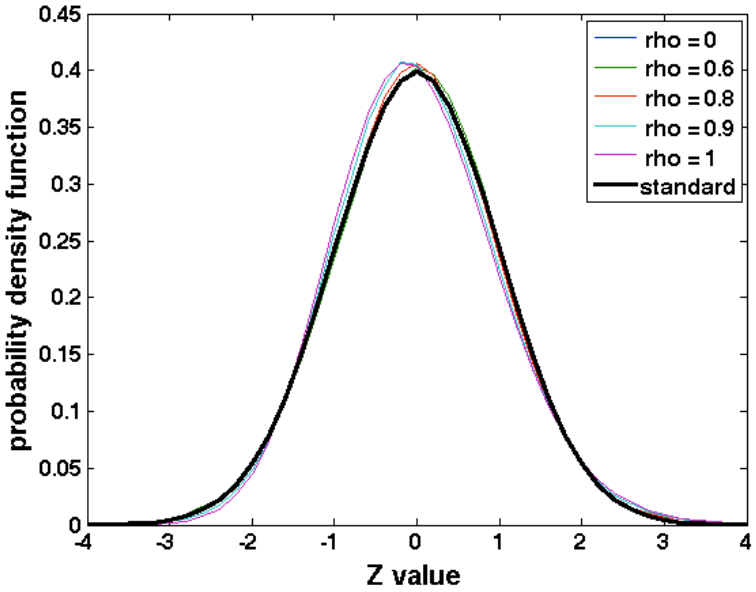

Fig. S2.1 Simulated null distributions of $\overline{Y_{k\approx 20}}$ under different ρs. In each simulation trial, time series X and Y (126 time frames, $k \approx 20$) with joint Gaussian distribution $\mathbb{N}\left(\begin{bmatrix}0\\0\end{bmatrix}, \begin{bmatrix}1 & \rho\\ \rho & 1\end{bmatrix}\right)$ are generated. $\overline{Y_k}$ is calculated by averaging those time frames during which X is > 1. 2*10^6 trials are simulated for each ρ. Distributions of the scaled $\overline{Y_k}$ (demeaned and divided by the standard deviation) are compared against the standard normal distribution (black line).

S2.3 CAPs solely associated with *SEED1/SEED2*

Briefly, regions demonstrating positive amplitudes in *SEED1/SEED2-CAPs* mirrored the correlation patterns shown in Fig. 1 (main text) to some extent but exhibited subtle differences. Compared to *SEED1-DMN*, the MPFC decoupled with PCC/precuneus; regions in DLPFC (part of the salience network as defined in FINDlab functional atlas) and executive control network became prominent in *SEED1-CAP*. By contrast, *SEED2-CAP* closely resembled *SEED2-DMN* (Fig. 1, main text).

Regions exhibiting significant negative amplitudes in *SEED2-CAP* were akin to the anti-correlated areas generated by linear correlation with the whole scan time points. No regions with clear structures from *SEED1-CAP* survived the statistical threshold (FDR corrected, $p < 0.05$).

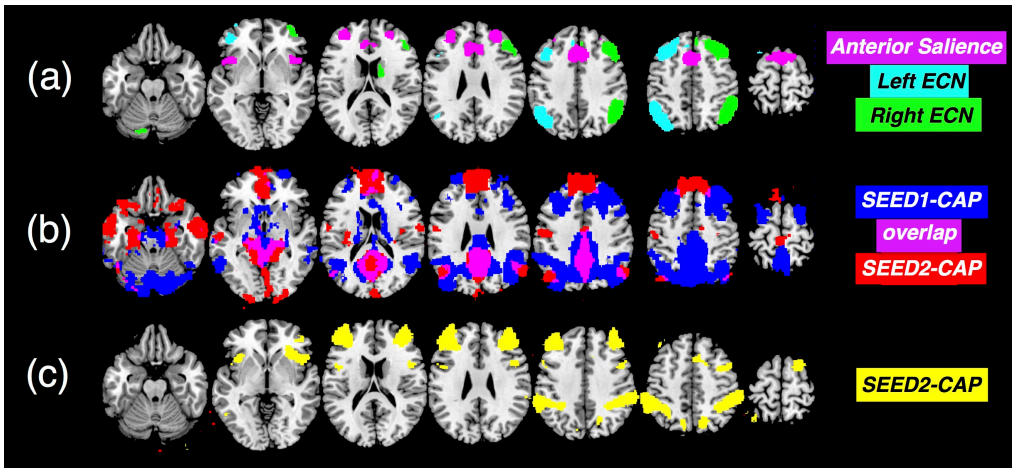

Fig. S2.2 (a) Functional Salience and Executive Control Network atlas reported by Stanford FINDlab. (b) Regions exhibiting significant positive BOLD contrasts in *SEED1/SEED2-CAPs* (group-level results, FDR corrected, $p < 0.01$). (c) Regions exhibiting significant negative BOLD contrasts in *SEED2-CAP* (group-level results, FDR corrected, $p < 0.05$). Since no regions with clear structures from *SEED1-CAP* survived the statistical threshold (FDR corrected, $p < 0.05$), results are not shown.

S2.4 Influence of preprocessing steps on CAPs solely associated with *SEED1/SEED2*

Fig. S2.2 were also re-analyzed without RETROICOR/RVHRCOR correction ('*none*') and with global signal regression ('*gsr*') to assess the influence of preprocessing steps, the results were presented in Fig. S2.3 below.

In the '*none*' case, the derived CAPs and their derivation from linear correlation results were in line with Fig. S2.2 above. In the '*gsr*' case, both *SEED1/SEED2-CAPs* were very similar to the linear correlation results (Fig. 1 '*gsr*', main text), thresholded with higher cutoff t-scores. The diminished divergence between CAP results (only focusing on moments when two seeds dissociated with each other) and linear functional connectivity (integrating the entire scan data) in '*gsr*', may be attributed to reduced temporal synchrony between *SEED1* and *SEED2* post GSR (linear Pearson correlation coefficient $r = 0.48 \pm 0.22$ across 20 subjects, compared to $r = 0.60 \pm 0.19$ with RETROICOR/RVHRCOR correction and $r = 0.61 \pm 0.18$ with '*none*').

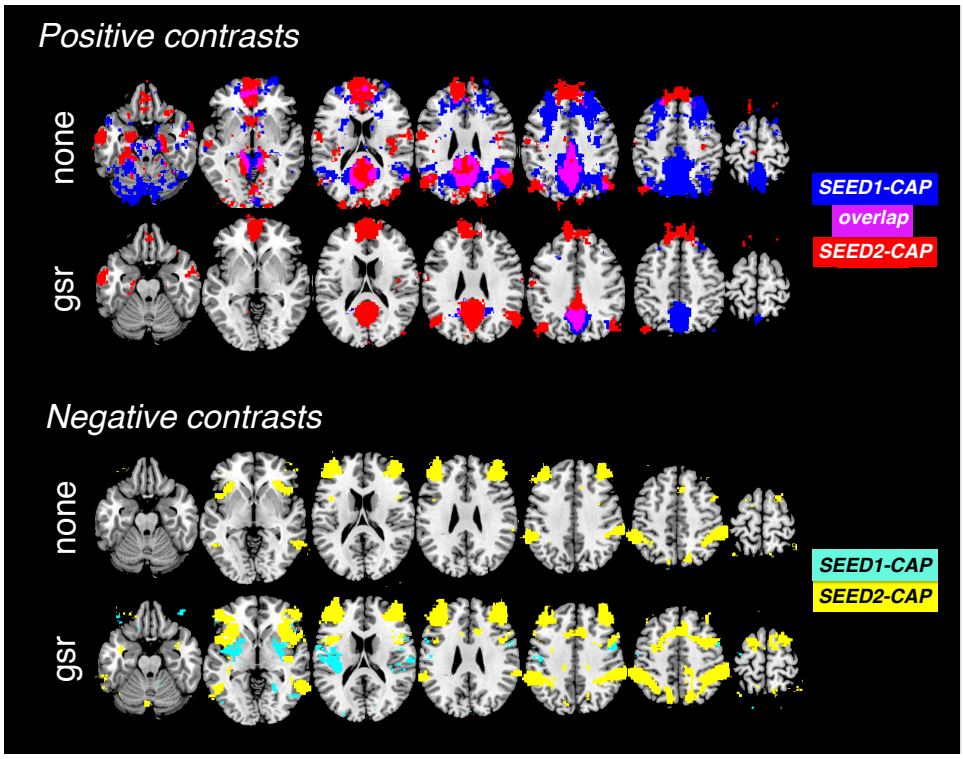

Fig. S2.3 Influence of preprocessing on *SEED1/SEE2-CAPs* (definition of *'none'* and *'gsr'* are identical as Fig. 1). Positive contrasts are thresholded by $p < 0.01$ and negative contrasts are thresholded by $p < 0.05$, FDR corrected. In the '*none*' case, no regions from *SEED1-CAP* survived the statistical threshold of negative contrasts.

S3 Re-analyses of results using Talairach coordinate system

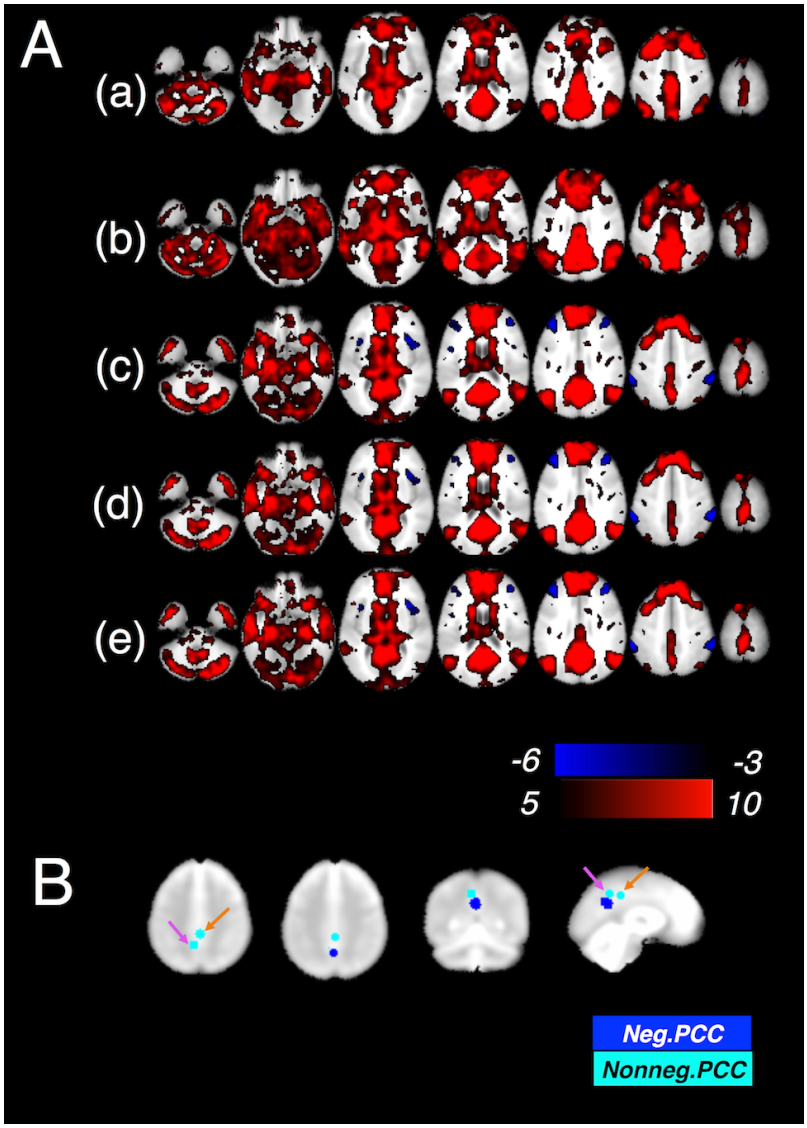

Fig. S3.1 Positive/negative correlations with PCC seeds reported by previous studies (Talairach coordinate system, *model-based physiological correction*). In lieu of converting Talairach PCC coordinates to the MNI coordinate system, subjects' datasets were transformed to the Talairach coordinates (BOLD images were normalized to the TT_EPI.nii template offered by AFNI http://afni.nimh.nih.gov/afni/). (A) Regions positively-/negatively correlated with PCC seeds reported by previous literature (Table 1 in main text, group-level t-map). (B) Coordinates of PCC seeds (spheres with radius = 6mm), '*Neg.PCC*'/'*Nonneg.PCC*' denote seed coordinates from studies observing/failing to observe significant anti-correlations between the DMN and TPN respectively. The seeds employed in Murphy *et al.* 2009 and Fox *et al.* 2009[1] are highlighted with *magenta* and *orange arrows*, respectively.

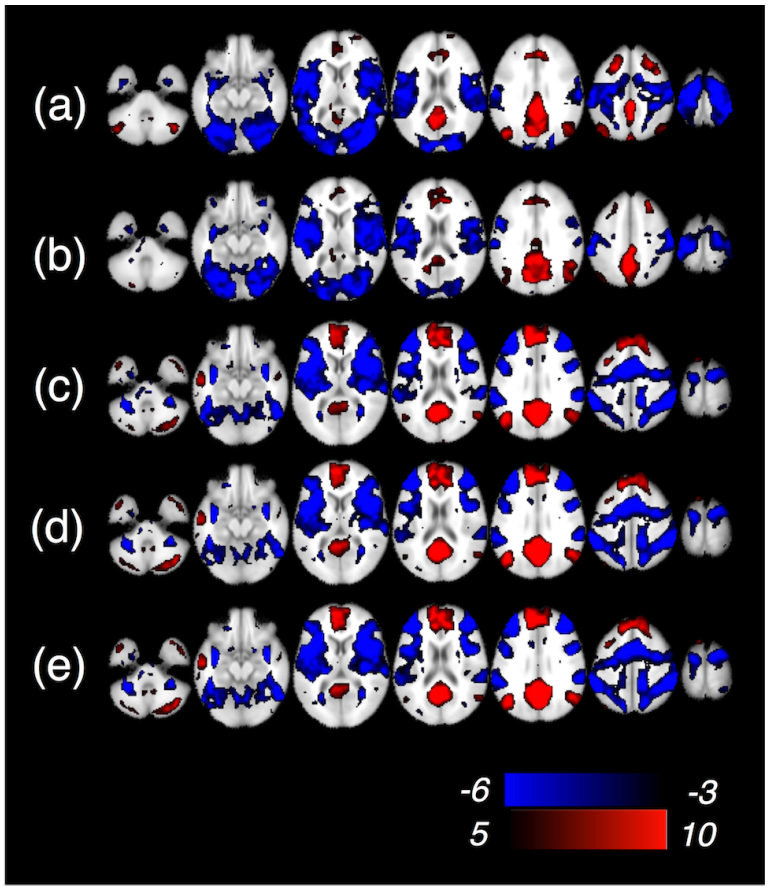

Fig. S3.2 Regions positively-/negatively correlated with PCC seeds reported by previous literature (same as Fig. S3.1 A, Talairach coordinate system, *global signal regression*).

S4 Influence of low-pass filtering on DMN correlations/anti-correlations

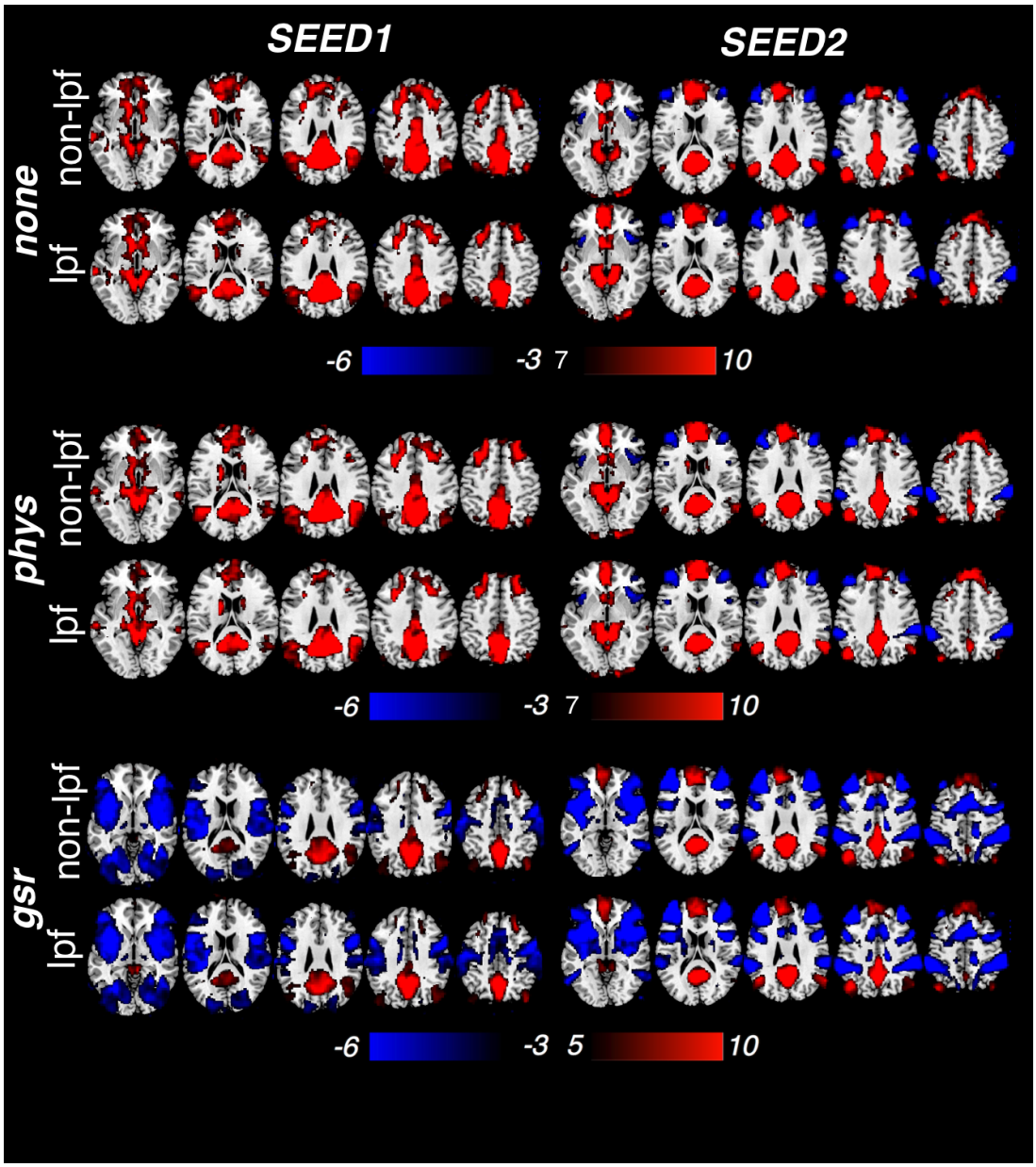

Fig. S4 Influence of low-pass filtering (< 0.1 Hz) on PCC correlations/anti-correlations (group-level t-score map, 'lpf': with low-pass filtering, 'non-lpf': without low-pass filtering). Results of Fig. 1 in the main text were re-analyzed by including low-pass filtering in preprocessing. The display thresholds of positive t-scores ('*none*' and '*phys*') are higher than Fig. 1 so that slight decrease in positive correlations can be better perceived.

S5 Datasets from a separate study investigating the effects of caffeine on the power spectra of resting state neural networks, 8-min resting state scans from healthy controls prior to administration of placebo.

15 healthy subjects (6 females), aged 29±5 years, were employed. The scan environment (scanner and sequence) was identical as the datasets examined in the main text. Thirty-one axial slices were acquired with 4-mm slice thickness, 0.5mm-skip (TR = 2000 ms, TE = 30 ms, flip angle = 80° , matrix 64×64, FOV = 22 cm). Respiration and cardiac (pulse oximetry) data were recorded using the scanner's built-in physiological monitoring system.

Preprocessing steps are identical as in section 2.2 of the main text.

S5.1 Motion and physiological data

The peak-to-peak and RMS excursion of motion were 0.44±0.32 mm, 0.13±0.07 mm (mean±SD) respectively. The mean and standard deviation of heart rate were 61.2±9.4 beat/min and 3.86±2.15 beat/min. The averaged rate of respiration was 15.2±2.5 cycle/min. The 'variation' of respiratory volume was 17.8±4.2 %.

No prominent differences could be observed between this dataset and those in the main text except the mean of heart rate ($p = 0.01$, uncorrected).

S5.2 FMRI results

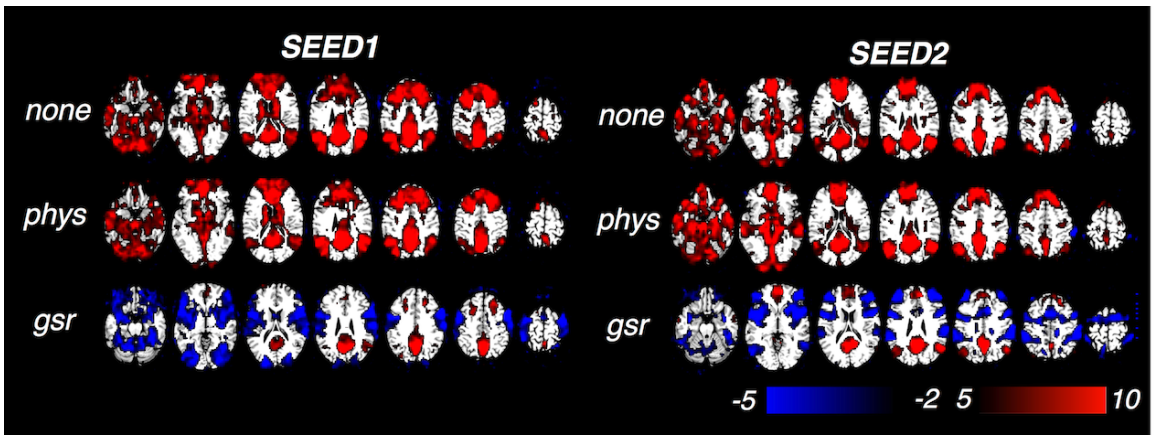

Fig. S5.2.1 Regions positively/negatively correlated with two PCC seeds (group-level t-score map). *'none'*: standard preprocessing (2.2 Data preprocessing, main text) without model-based physiological noise correction (RETROICOR, RVHRCOR); *'phys'*: standard preprocessing; *'gsr'* global signal regression without any additional physiological noise correction.

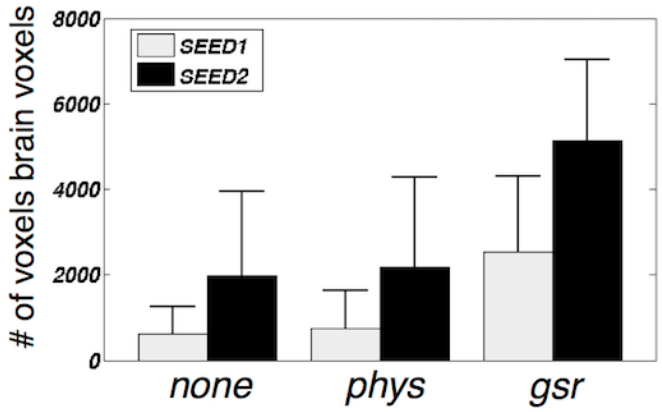

Fig. S5.2.2 Number of voxels negatively correlated with *SEED1/SEED2* (correlation coefficient $r < -0.2$) under different preprocessing conditions. P values from paired-t tests (# of voxels negatively correlated with *SEED1* vs. *SEED2*) under '*none/phys/gsr*' are 0.0133, 0.0138 and $1.1*10^{-5}$ respectively.

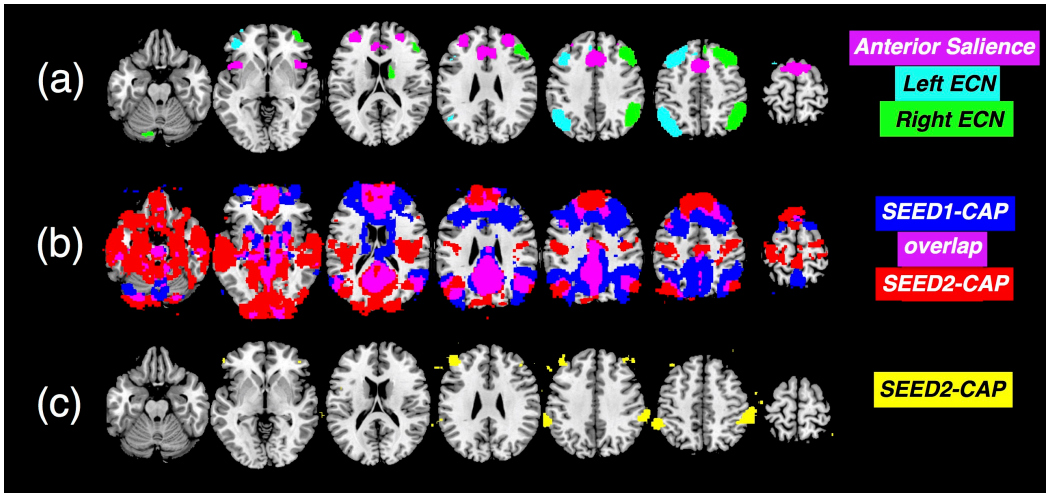

Fig. S5.2.3 (a) Functional Salience and Executive Control Network atlas reported by Stanford FINDlab. (b) Regions exhibiting significant positive BOLD contrasts within *SEED1/SEED2-CAPs* (group-level results, FDR corrected, $p < 0.01$). (c) Regions exhibiting significant negative BOLD contrasts averaged within *SEED2-CAP* (group-level results, FDR corrected, $p < 0.05$). Since no regions with clear structures from the *SEED1-CAP* survived the statistical threshold (FDR corrected, $p < 0.05$), results are not shown.

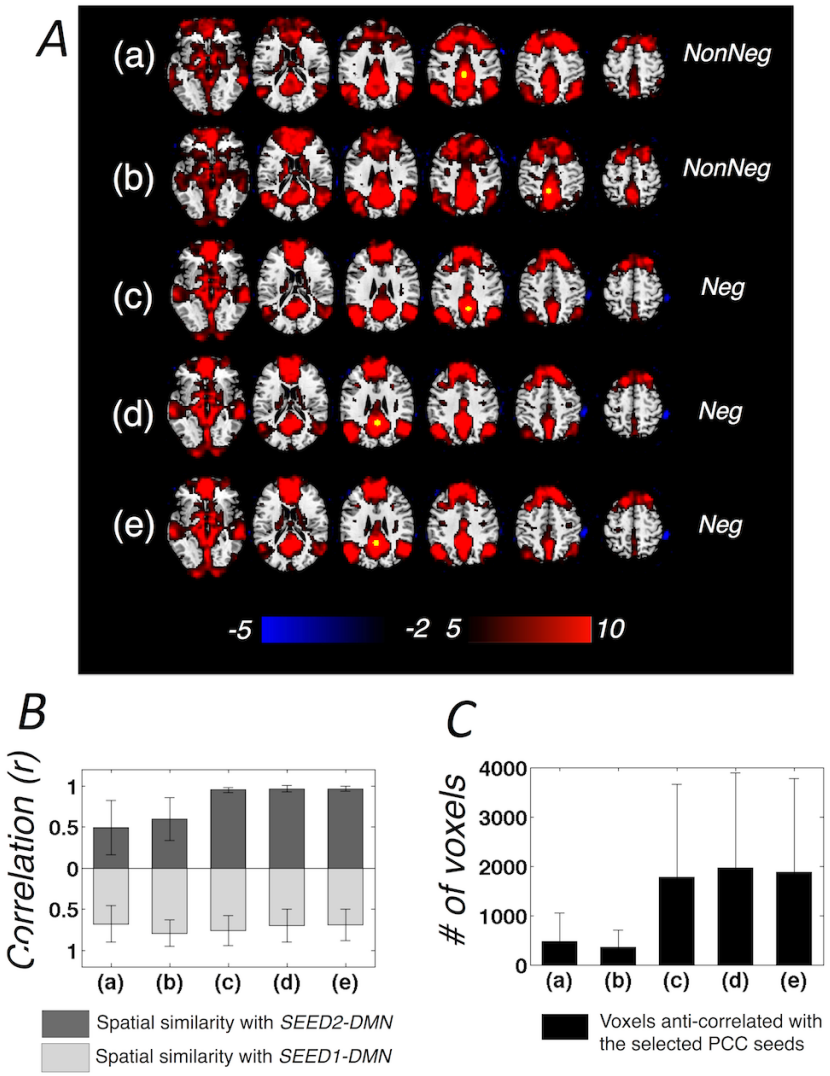

Fig. S5.2.4 (A) Regions positively/negatively correlated with PCC seeds reported by previous literature (Table 1, group-level t-map), seed locations are highlighted in yellow of each panel. (B) Spatial similarity (linear Pearson correlation between gray matter voxel intensity) between the DMN patterns derived in (A) and *SEED1-/SEED2-DMN*, mean and standard deviation estimated across all the subjects; (C) Number of voxels anti-correlated with PCC (correlation coefficient $r < -0.2$), mean and standard deviation estimated across all the subjects.

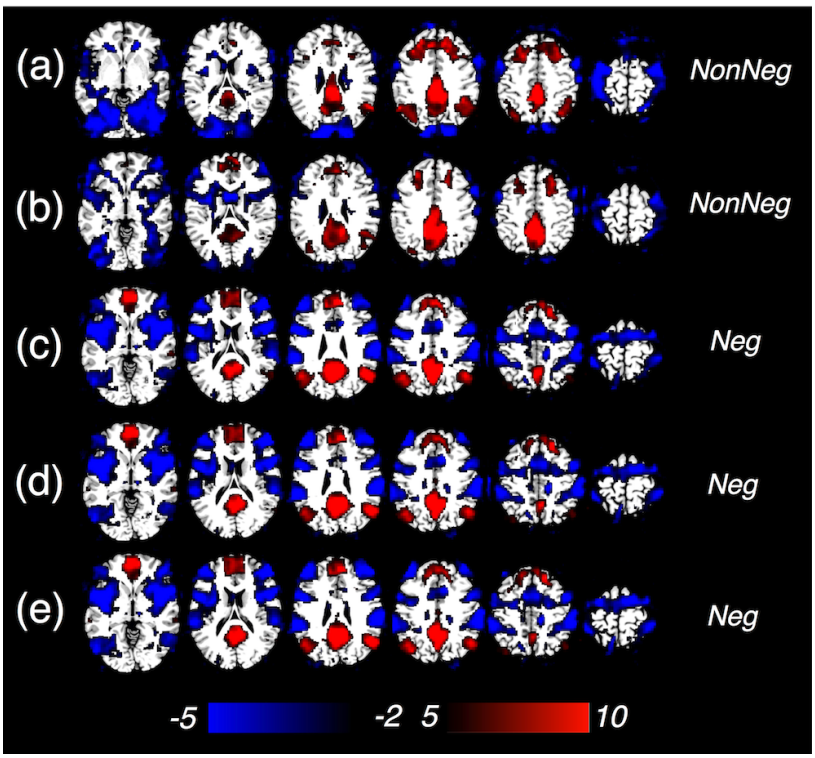

Fig. S5.2.5 Regions positively-/negatively correlated with PCC seeds reported by previous literature (similar to Fig. 5 in the main text, including *global signal regression* as a preprocessing step).

S6 PCC/precuneus correlation maps reported by the neurosynth online platform.

This online platform displays RS functional connectivity for the seed region in a sample of 1,000 subjects (ages 18–35 yr, scanned at Harvard and the Massachusetts General Hospital). In this dataset, data were low-pass filtered below 0.08 Hz, after GSR only, see (Buckner, et al., 2011; Choi, et al., 2012; Yeo, et al., 2011) for detailed descriptions of data analysis; while in our dataset, no low-pass filtering was performed, analysis was done with either model-based physiological noise correction or GSR. Five PCC/coordinates (Table 1) were tested and shown below. Consistent with findings in the main text, the resolved DMN patterns in the '*Neg*' group (Fig. S6 (c-e)) yield network patterns closely resembling the dDMN atlas, while '*NonNeg*' group seeds yield network patterns deviating from dDMN (Fig. S6 (a)) or closer to the vDMN (Fig. S6 (b)). Of note, anti-correlated networks from the '*Neg*' group are more extensive than the '*NonNeg*' group. These observations reconfirmed findings in the main text that different subnetworks of the DMN were examined across a number of studies.

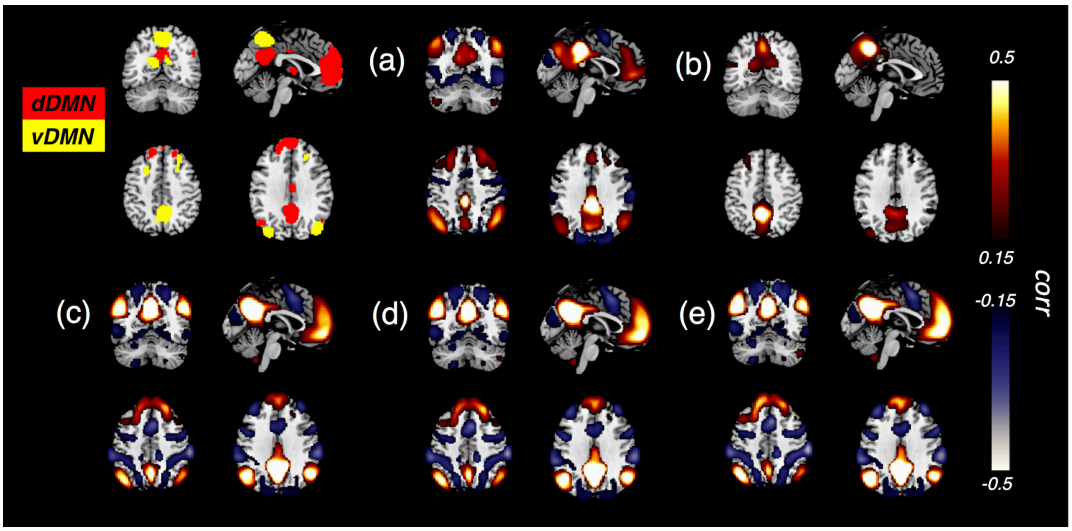

Fig. S6 Regions positively/negatively correlated with different PCC/precuneus seeds reported by studies listed in Table 1 (produced by the online platform neurosynth (with seed locations rounded even to match the input coordinate resolutions), data were low-passed filtered with the cut-off 0.08 Hz, after GSR. Figure labels are the same as the labels of studies in Table 1. Dorsal and ventral DMN functional atlas reported by the Stanford FIND lab (http://findlab.stanford.edu/functional_ROIs.html, derived using spatial ICA (Shirer et al., 2012)) are shown at the upper left for comparison.

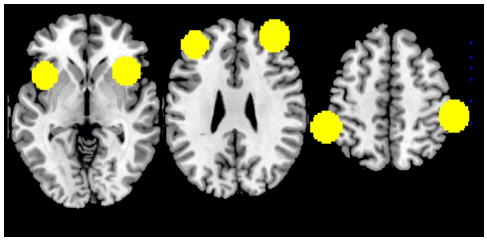

Fig. S7 Six TPN ROI masks (spheres with 15mm radius, in yellow) identified based on the 'phys' results shown in main text Fig. 1 (*SEED2-DMN*, covering bilateral insula, DLPFC and SMG, voxels with peak t-score values were selected as ROI centroids).

Table S1 Summary of each subject's functional and physiological metrics, and their correlation with the extent of DMN-TPN anti-correlations.
# of time frames: see main text section 2.5 for definition of TF_1 and TF_2, TF_0 refers to those time periods when both (*SEED1* z-score > 1 & *SEED2* z-score > 1);
r: linear Pearson correlation between the time courses of *SEED1* and *SEED2;*
physiological metrics: I: mean of heart rate (beat/min); II: standard deviation of heart rate (beat/min); III mean of respiratory rate (cycle/min); and IV variation of respiratory volume (%);
# of anti-correlated voxels: the number of voxels that are within the TPN mask (Fig. S7 above), and correlate negatively with *SEED2* (linear Pearson correlation $r < -0.2$);
p-val: the statistical significance of the linear Pearson correlation between each metric and the number of anti-correlated voxels.

(20 subjects in the main text)

Subject (*male)	# of time frames			r	Physiological Metrics				# of anti-correlated voxels
	TF_0	TF_1	TF_2		I	II	III	IV	
1*	10	27	28	0.30	80.2	2.6	20.2	16.4	5211
2	26	12	12	0.77	67.3	3.1	18.5	20.7	912
3	17	25	15	0.66	67.9	2.2	12.2	25.1	3428
4*	17	21	21	0.60	69.8	2.9	17.3	20.8	4689
5*	18	18	22	0.59	67.7	3.9	14.1	19.7	5395
6	10	31	22	0.28	66.7	2.6	20.4	8.1	3866
7	6	34	27	0.14	55.9	2.4	19.9	18.0	5790
8*	15	25	31	0.57	71.9	3.6	17.0	8.80	3342
9	24	15	16	0.81	53.3	6.9	14.5	16.6	3140
10*	29	11	24	0.68	69.8	2.9	18.7	9.8	7558
11*	33	12	10	0.81	50.4	3.0	18.0	13.5	2388
12*	26	21	12	0.74	64.9	2.4	20.4	15.0	3965
13*	15	23	23	0.60	53.6	4.2	15.2	18.2	2965
14*	8	25	26	0.37	47.9	2.6	16.2	11.5	2790
15	23	19	15	0.63	51.3	1.8	15.7	14.8	361
16	29	14	14	0.73	53.5	2.4	18.4	15.6	2641
17	22	22	15	0.66	64.4	2.6	16.0	5.30	4952
18	19	9	23	0.70	52.6	1.3	17.8	16.3	1412
19	22	22	22	0.61	79.3	1.9	16.9	13.6	174
20*	23	14	22	0.73	65.6	3.3	19.4	24.1	4736
p-val	0.38	0.35	0.12	0.17	0.23	0.39	0.36	0.79	

(15 subjects in the supplementary dataset)

Subject	# of time frames			r	Physiological Metrics				# of anti-correlated voxels
	TF0	TF1	TF2		I	II	III	IV	
1(F)	10	15	21	0.38	52.7	2.0	13.6	14.1	578
2	11	25	21	0.48	69.7	5.7	11.5	13.3	2611
3	24	12	9	0.79	58.7	2.2	15.8	18.2	1178
4	12	18	22	0.48	74.2	9.0	14.8	20.6	601
5	17	13	13	0.74	48.4	1.4	14.3	19.9	5056
6	21	12	9	0.76	57.4	2.8	16.3	9.9	467
7	14	17	17	0.54	58.3	5.7	16.9	16.8	402
8	17	15	16	0.74	58.6	2.4	20.1	14.2	9
9	13	20	18	0.68	70.9	3.8	12.6	21.5	322
10	25	17	15	0.80	59.2	2.0	17.1	21.2	1050
11	19	13	19	0.57	65.8	2.7	17.2	21.7	6832
12	11	24	17	0.61	63.6	6.6	17.9	23.3	4024
13	11	16	21	0.59	80.0	2.7	13.8	20.4	3468
14	13	17	21	0.68	51.7	2.9	15.0	20.5	4446
15	13	12	19	0.72	48.8	5.3	11.3	11.3	1573
p-val	0.81	0.96	0.52	0.88	1	0.58	0.98	0.07	

References:

Buckner, R.L., Krienen, F.M., Castellanos, A., Diaz, J.C., Yeo, B.T. 2011. The organization of the human cerebellum estimated by intrinsic functional connectivity. J Neurophysiol, 106:2322-45.

Cauda, F., Geminiani, G., D'Agata, F., Sacco, K., Duca, S., Bagshaw, A.P., Cavanna, A.E., 2010. Functional connectivity of the posteromedial cortex. PLoS One 5.

Choi, E.Y., Yeo, B.T., Buckner, R.L. 2012. The organization of the human striatum estimated by intrinsic functional connectivity. J Neurophysiol, 108:2242-63.

Margulies, D.S., Vincent, J.L., Kelly, C., Lohmann, G., Uddin, L.Q., Biswal, B.B., Villringer, A., Castellanos, F.X., Milham, M.P., Petrides, M., 2009. Precuneus shares intrinsic functional architecture in humans and monkeys. Proc Natl Acad Sci U S A 106, 20069-20074.

Rand, W.M., 1971. Objective criteria for the evaluation of clustering methods. Journal of the American Statistical Association 66, 5.

Shirer, W.R., Ryali, S., Rykhlevskaia, E., Menon, V., Greicius, M.D., 2012. Decoding subject-driven cognitive states with whole-brain connectivity patterns. Cerebral cortex 22, 158-165.

Yeo, B.T., Krienen, F.M., Sepulcre, J., Sabuncu, M.R., Lashkari, D., Hollinshead, M., Roffman, J.L., Smoller, J.W., Zollei, L., Polimeni, J.R., Fischl, B., Liu, H., Buckner, R.L.

2011. The organization of the human cerebral cortex estimated by intrinsic functional connectivity. J Neurophysiol, 106:1125-65.
Zhang, Y., Fan, L., Zhang, Y., Wang, J., Zhu, M., Zhang, Y., Yu, C., Jiang, T., 2014. Connectivity-based parcellation of the human posteromedial cortex. Cereb Cortex 24, 719-727.